



OPEN

Cell type- and layer-specific plasticity of olfactory bulb interneurons following olfactory sensory neuron ablation

Tenzin Kunkhyen¹, Taryn R. Brechbill^{1,2}, Sarah P. R. Berg^{1,2}, Pranitha Pothuri¹, Alexander N. Rangel¹, Ashna Gupta¹ & Claire E. J. Cheetham¹✉

Lifelong neurogenesis endows the mouse olfactory system with a capacity for regeneration that is unique in the mammalian nervous system. Throughout life, olfactory sensory neurons (OSNs) are generated from olfactory epithelium (OE) stem cells in the nose, while the subventricular zone generates neuroblasts that migrate to the olfactory bulb (OB) and differentiate into multiple populations of inhibitory interneurons. Methimazole (MMZ) selectively ablates OSNs, but OE neurogenesis enables OSN repopulation and gradual recovery of OSN input to the OB within 6 weeks. However, it is not known how OB interneurons are affected by this loss and subsequent regeneration of OSN input following MMZ treatment. We found that dopaminergic neuron density was significantly reduced 7–14 days post-MMZ but recovered substantially at 35 days. The density of parvalbumin-expressing interneurons was unaffected by MMZ; however, their soma size was significantly reduced at 7–14 days post-MMZ, recovering by 35 days. Surprisingly, we found a transient increase in the density of calretinin-expressing neurons in the glomerular and external plexiform layers, but not the granule cell layer, 7 days post-MMZ. This could not be accounted for by increased neurogenesis but may result from increased calretinin expression. Together, our data demonstrate cell type- and layer-specific changes in OB interneuron density and morphology after MMZ treatment, providing new insight into the range of plasticity mechanisms employed by OB circuits during loss and regeneration of sensory input.

Postnatal neurogenesis is rare in the mammalian nervous system. However, in the mouse olfactory system, multiple populations of neurons are generated throughout life from stem cells in two distinct locations: the olfactory epithelium (OE) and the subventricular zone (SVZ). This endows the olfactory system with substantial regenerative capacity and provides a unique opportunity to understand the mechanisms by which endogenously generated stem cell-derived neurons integrate into healthy and regenerating circuits in the brain.

The SVZ generates neuroblasts that migrate via the rostral migratory stream (RMS) to the olfactory bulb (OB), where they differentiate into multiple molecularly distinct sub-populations of interneurons located primarily in the glomerular layer (GL) and granule cell layer (GCL)^{1–3}. Surprisingly, with the notable exception of the dopaminergic (DA) neurons, how most OB interneuron types are impacted by changes in sensory input from the OE is poorly understood. An early study found that naris occlusion in either neonatal or young adult rats reduced the density of calbindin-expressing (CB+) but not calretinin-expressing (CR+) periglomerular cells (PGCs) and reduced the density of parvalbumin-expressing (PV+) interneurons, which are found predominantly in the external plexiform layer (EPL)⁴. A more recent study found that naris occlusion in adult mice did not affect the survival of pre-existing CB+ or CR+ PGCs or the fate specification of newborn CB+ and CR+ PGCs⁵. Hence, there is somewhat conflicted evidence for activity-dependent changes, especially in PGCs.

In contrast, the effects of blocking sensory input on DA neurons have been studied extensively. DA neurons are found mainly in the GL but also scattered in the EPL and play multiple important roles in odor processing, including inhibition, gain control and decorrelation of odor representation in OB output neurons^{6,7}, inhibition of PGCs and dual inhibitory-excitatory modulation of external tufted cells surrounding distant glomeruli^{8,9}, and reducing OSN release probability^{10–13}. It has long been known that both dopamine production and expression

¹Department of Neurobiology, University of Pittsburgh, Pittsburgh, PA 15213, USA. ²These authors contributed equally: Taryn R. Brechbill and Sarah P. R. Berg. ✉email: cheetham@pitt.edu

of tyrosine hydroxylase (TH), the rate-limiting enzyme for dopamine biosynthesis, are strongly reduced when sensory input is blocked via either olfactory epithelium lesion or naris occlusion^{14–17}. TH expression levels do recover to baseline levels after restoration of sensory input^{15,18}. More recently, using Cre recombination-based labeling strategies that indelibly mark DA neurons and hence circumvent activity-dependent changes in TH expression, it has been shown that DA neuron survival is also reduced by a four-week naris occlusion^{18,19}. However, the magnitude of DA neuron cell death varied widely between these two studies: 40% in Sawada et al.¹⁹, vs. 5% in Angelova et al.¹⁸. Nonetheless, both studies found that four weeks of restored sensory input was sufficient for DA neuron density to recover to baseline^{18,19}, suggesting the incorporation of newly generated DA neurons. Notably, however, the effect of OE damage on DA neuron survival and neurogenesis remains unknown.

Sensory input to the OB is provided by olfactory sensory neurons (OSNs), which are themselves generated throughout life from basal stem cells located in the OE. OSNs can be generated from both globose and horizontal basal cells, with the latter playing an important role following OE damage^{20–22}. Notably, naris occlusion in adult mice does not alter OSN density or neurogenesis²³, suggesting that the impact of naris occlusion vs. OE damage on OB interneurons may be very different. Methimazole (MMZ) treatment has emerged as an interesting model in which sensory input to the OB is abruptly lost and then gradually regenerates. A single dose of MMZ pharmacologically ablates OSNs without damaging basal stem cells, such that the OE is repopulated with OSNs within 4–6 weeks^{24–26}. Regeneration of sensory input to the OB begins within a week, with the first immature OSNs generated after MMZ treatment providing sufficient sensory input to permit recovery of odor detection and even some simple odor discrimination behavior²⁷. Over longer time periods, it has been shown that OSN inputs to external tufted cells return in 16 days²⁵, and behavior in a previously learnt odor discrimination task recovers within 45 days²⁶, following MMZ treatment. Determining how MMZ impacts the size of OB interneuron populations can therefore provide important insight into their survival and the extent to which adult neurogenesis can restore depleted neuron populations.

Our goal in this study was to determine the effects of MMZ treatment on OB interneuron survival and regeneration, focusing on three interneuron subtypes. DA neurons (TH+) were selected due to their strong dependence on sensory input for TH expression and survival and their ability to repopulate following naris occlusion. PV+ neurons were of interest because a large activity-dependent reduction in their density has been reported⁴, yet they are not normally generated in adults. Indeed, in mice, most PV+ neurons are generated during late embryonic and early postnatal life, with neurogenesis ceasing as early as postnatal day (P)7^{28,29}, suggesting that lost PV+ neurons cannot be replaced. PV+ neurons form dense reciprocal connections with mitral and tufted cell dendrites^{30–34} and are thought to modulate OB output gain³²; hence, changes in their density could have an important impact on OB output. Finally, CR+ neurons were selected because they are the most abundant subtype of adult-born OB neurons^{28,35}, comprise both PGC and granule cell (GC) populations, and are generated not only in the SVZ but also in the core of the OB itself and possibly the rostral migratory stream^{36–41}.

Calretinin-expressing (CR+PGCs are the most numerous subtype of GL interneurons^{42–44} and are mostly generated postnatally^{28,29,35,45}. They express an unusually restricted range of voltage-gated channels, resulting in very high input resistance and firing of at most one action potential in response to depolarizing current injection^{46,47}. They also receive few synaptic inputs and may not form functional output synapses^{47,48}. As a result, their function remains enigmatic, although it has been suggested that they improve signal:noise ratio at an early stage of olfactory processing by inhibiting principal neuron responses to asynchronous signals⁴⁶. A significant fraction of superficial GCs also express CR; their neurogenesis peaks around birth but persists into adulthood^{28,29}. CR+ GCs are morphologically similar to surrounding GCs, and receive similar excitatory inputs, but fewer inhibitory inputs than other GC types⁴⁹. CR+ GCs are preferentially activated during odor discrimination and contribute to fine odor discrimination learning⁴⁹.

We found that TH+ neuron density underwent bidirectional changes in the 5 weeks following MMZ treatment, validating the loss and subsequent regeneration of OB sensory input. While PV+ neuron density was unaffected by MMZ treatment, PV+ soma area was strongly reduced 7–14 days post-MMZ but recovered within 35 days. Surprisingly, there was a transient increase in CR+ neuron density at 7 days post-MMZ only in the GL and EPL. Together, our data demonstrate cell type- and laminar-specific changes in response to MMZ treatment, indicating the broad range of plasticity mechanisms, including but not limited to neurogenesis, available in the adult mouse OB.

Methods

Experimental animals

All procedures followed NIH and ARRIVE guidelines and were approved by the University of Pittsburgh Institutional Animal Care and Use Committee. C57BL/6J mice (strain #000664) were purchased from The Jackson Laboratory and/or bred in-house, with new breeders purchased every 12 months to minimize genetic drift. Mice were maintained in individually ventilated cages at 22 °C and 48% humidity on a 12 h light/dark cycle with unrestricted access to food and water. Mice were group-housed unless same sex littermates were unavailable. A total of 71 mice were used in this study.

Methimazole and EdU treatment

For analysis of neuronal density, 8-week-old C57BL/6J mice received an intraperitoneal (IP) injection of 75 mg/kg MMZ (EMD Millipore), dissolved in sterile saline, or an equivalent volume of sterile saline. Mice were perfused 3, 7, 14 or 35 days after injection with MMZ or saline. For analysis of CR+ EdU+ neuron density, 8-week-old C57BL/6J mice received an IP injection of MMZ, then an IP injection of 50 mg/kg 5-ethynyl-2'-deoxyuridine (EdU (ThermoFisher Scientific)) 24 h later and were perfused after a further 6 days.

Transcardial perfusion and cryosectioning

Mice were deeply anesthetized with 5% isoflurane in 1 l/min oxygen or with 200 mg/kg ketamine and 20 mg/kg xylazine, then transcardially perfused with ice-cold phosphate-buffered saline (PBS) and then 4% paraformaldehyde (PFA) in PBS. OEs and OBs were dissected and post-fixed overnight, then cryopreserved in 30% sucrose, embedded in 10% gelatin, and fixed/cryopreserved overnight in 15% sucrose/ 2% PFA. Gelatin blocks were flash-frozen in 2-methylbutane on dry ice and stored in a -80 °C freezer. Coronal sections were cut at 50 µm for the OE and 40 µm for the OB using a cryostat.

Immunohistochemistry and EdU staining

Free-floating OE and OB sections were treated with 1% sodium borohydride, washed with PBS, then blocked/permeabilized (5% normal donkey serum [NDS]/0.5% Triton X-100 in PBS) for 1 h. Sections were incubated with primary antibody diluted in 3% NDS, 0.2% Triton X-100, 0.01% sodium azide in PBS as shown in Table 1. After washing in PBS, sections were incubated in secondary antibody solution (Table 1; diluted in 3% NDS, 0.2% Triton X-100 in PBS) for 1 h at room temperature. Sections were washed in PBS and mounted with Vectashield containing DAPI (Vector Labs). One set of OB sections was used for staining with each interneuron primary antibody (to detect TH, CR and PV, respectively). OE sections were stained with primary antibodies to detect growth-associated protein 43 (GAP43; a marker for immature OSNs) or olfactory marker protein (OMP; a marker for mature OSNs).

OB sections from mice that had been injected with MMZ or saline and EdU underwent CR staining as described above, followed by EdU staining modified from Goedhart⁵⁰. Briefly, these sections were permeabilized in 0.5% Triton X-100 in PBS for 30 min, then incubated with 200 mM copper sulfate, 4 mM sulfo-Cyanine5-azide (#A3330, Lumiprobe) and 114 mM ascorbic acid in PBS for 30 min in the dark. Sections were washed in 0.5% Triton X-100 in PBS and mounted.

Confocal microscopy

Images of stained OE sections were acquired using a Nikon A1R confocal microscope with an Apo 60x/1.4 NA oil immersion objective and Elements software (Nikon). Laser excitation and bandpass emission filters were 405 nm and 450/50 for DAPI, and 561 nm and 595/50 for OMP-AF568 or GAP43-AF568. We confined imaging to the septal OE to control for anatomical variations such as concha bullosa.

Widefield fluorescence microscopy

Tiled images of stained whole OB sections were acquired using either an Eclipse 90i microscope with a Plan Apo 10x/0.45 NA air objective, motorized stage and Elements Software (Nikon), or a Revolve microscope with Echo software (Echo), a Plan Apo 10x/0.4 NA air objective (Olympus) and Affinity Photo software (Affinity) for image stitching. Bandpass excitation/emission filter wavelengths were (in nm): DAPI (385/30, 450/50); unstained green (470/40, 525/50); TH-, PV- or CR-AF546 (530/40, 590/50); EdU-AF647 (640/30, 690/50). We collected DAPI, green (unstained) and AF546 channels for analysis of TH+, PV+ and CR+ neuron density. We collected DAPI, CR-AF488, red (unstained) and EdU-AF647 channels for analysis of CR+ EdU+ neuron density and CR fluorescence intensity. Detection settings were identical for all images collected for this data set.

Image analysis

Image analysis was performed using Fiji (ImageJ)⁵¹. Anterior, central and posterior OB sections, which were approximately 25, 50 and 75% along the anterior–posterior axis, were selected for analysis of TH+, PV+ and

Antibody	Dilution	Species	Incubation conditions	RRID	Manufacturer Catalog #
OMP	1:5000	Goat	96 h 4 °C	AB_664696	Wako 544–10,001
GAP43	1:1000	Rabbit	96 h 4 °C	AB_10001196	Novus NB300-143
Tyrosine hydroxylase	1:2500	Rabbit	48 h 4 °C	AB_10077691	Novus NB300-109
Calretinin	1:500	Rabbit	96 h 4 °C	AB_2068506	Millipore Sigma AB5054
Parvalbumin	1:500	Mouse	48 h 4 °C	AB_2174013	Millipore Sigma MAB1572
Calretinin	1:500	Mouse	96 h 4 °C	AB_94359	Millipore Sigma MAB1568
Goat-AF546	1:500	Donkey	1 h room temperature	AB_2534103	ThermoFisher A-11056
Rabbit-AF546	1:500	Donkey	1 h room temperature	AB_2534016	ThermoFisher A10040
Mouse-AF546	1:500	Donkey	1 h room temperature	AB_11180613	ThermoFisher A10036

Table 1. Primary and secondary antibodies used.

CR+ neuron density. OB layers were outlined in the DAPI channel of each section and used to demarcate regions of interest for cell counting or fluorescence intensity analysis. The area of each layer was measured, and neurons were counted manually within each layer using the multi-point tool. Neurons were not counted if they partially crossed the border with an adjacent layer. We confined our analysis to layers that had been shown previously to contain a significant density of TH+ (GL and EPL), PV+ (EPL, MCL/IPL, GCL) or CR+ (GL, EPL, GCL) neurons. We removed potential contamination due to autofluorescence of lipofuscin granules, which are prevalent in the GL, by ensuring that counted neurons were only present in the CR or TH channel and not in the unstained channel. Neuronal density was then calculated for each layer.

We measured PV+ neuron soma area only in the EPL, where PV+ neuron density³² is high enough to enable consistent sampling. We drew polygonal regions of interest (ROIs) around a total of 20 randomly selected PV+ neurons per OB section (five each in the dorsal, ventral, medial and lateral EPL). This was completed for the EPL of all images used for PV+ neuron density analysis.

For analysis of CR+ EdU+ neuron density, the GL and EPL were outlined, and their areas measured. Neurons that were both CR+ and EdU+ were marked using the multi-point tool, and their density was calculated. To determine the proportion of EdU+ cells that express CR, the total EdU density was calculated by counting the total number of EdU+ cells within the same outlined regions for the GL and EPL. The background-subtracted mean fluorescence intensity of CR staining was also determined for the GL and EPL in these images.

Modeling of PV+ neuron excitability

We used a leaky integrate and fire model in Matlab 2018b (Mathworks) to determine the number of action potentials elicited by 300 ms square depolarizing current pulses (200–400 pA). Parameters for PV+ neurons were either stated in, or derived from action potential firing traces provided in, Kato et al.³²: resting membrane potential – 60 mV; spike threshold – 35 mV; post-spike voltage – 60 mV; membrane time constant (τ) 5.9 ms; and input resistance 91 M Ω (for saline-treated mice). As soma area was very similar between 7- and 14-day post-MMZ groups, we used to the soma area of 7-day post-MMZ PV+ neurons, which resulted in an input resistance of 121 M Ω . The difference in input resistance was calculated from the difference in soma area between PV+ neurons from saline- and MMZ-treated mice given that $\tau = \text{input resistance} \times \text{capacitance}$, $\text{input resistance} = \text{membrane resistance} / \text{membrane surface area}$ and $\text{capacitance} = \text{membrane capacitance} \times \text{membrane surface area}$. The model assumes no difference in the dendritic arbors of PV+ neurons in saline vs. MMZ-treated mice. Rheobase was defined as the minimum current that elicited action potential firing. We note that the model captures the non-adapting high frequency firing reported for OB PV+ neurons but does not fully recapitulate their firing pattern in terms of a gap following initial spikes before high frequency firing resumes³².

Statistics

Statistical analysis was performed using Prism 10 (GraphPad). All data sets passed the Shapiro–Wilk test for normality. All data sets were compared using 2-way ANOVA and Sidak's multiple comparisons tests, with $\alpha = 0.05$.

Results

Repopulation of OSNs in the OE 5 weeks after MMZ treatment

A single dose of MMZ has previously been shown to selectively ablate virtually all OSNs in the OE^{24,27,52–54}. OSN neurogenesis from the preserved population of both globose basal cells and the normally quiescent horizontal basal cells then repopulates OSNs within four weeks^{21,24,55,56}. Based on this, we selected time points 7, 14 and 35 days after MMZ treatment to study changes in OB interneuron populations as OSNs are lost and then repopulate. We first assessed the extent of OSN repopulation at these time points (Fig. 1). We found that OSNs were ablated by MMZ treatment (Fig. 1b), with GAP43+ OSNs returning by 7 days post-MMZ (Fig. 1b,c) and an increased number of GAP43+ and some OMP+ OSNs present at 14 days post-MMZ (Fig. 1d). By 35 days post-MMZ, significant repopulation of both immature and mature OSNs had occurred (Fig. 1a,e). We concluded that MMZ treatment provides a model of degeneration and subsequent regeneration of OSNs, and hence sensory input to the OB, that would enable us to study the impact of these changes on OB interneuron populations.

Recovery of TH+ neuron density five weeks after MMZ treatment

We first assessed changes in the density of OB neurons expressing TH, the rate limiting enzyme in dopamine biosynthesis and a marker for one of the three major subtypes of inhibitory juxtglomerular neurons in mice^{57,58}. TH expression is known to be strongly dependent on sensory input in OB dopaminergic neurons^{14–16,59}. As reported previously^{15,60}, we observed a high density of TH+ neurons in the GL as well as a lower density in the EPL (Fig. 2). Therefore, we focused our analysis on those two layers. TH+ neuron density was significantly reduced in both the GL and EPL at 7 and 14 days after MMZ injection relative to saline controls (Fig. 2b–e; Fig. 3a–d; GL: 53% lower at 7 days, 46% lower at 14 days; EPL: 29% lower at 7 days, 25% lower at 14 days). However, by 35 days after MMZ treatment, TH+ neuron density in both the GL and the EPL had recovered and was no longer significantly different to that in saline-treated mice (Fig. 2f,g; Fig. 3e,f). We found no effect of position along the anterior–posterior axis on the pattern of MMZ-related changes (Fig. 3).

MMZ treatment does not affect OB PV+ neuron density but reduces PV+ soma area

We then asked whether the density of OB PV-expressing interneurons was affected by MMZ treatment. PV+ neurons are normally generated only during embryonic and early postnatal development²⁸. However, it has been unclear whether PV+ neuron survival is affected by sensory input or whether injury can induce PV+ neurogenesis. We performed PV staining in anterior, central and posterior OB sections from mice that had been injected

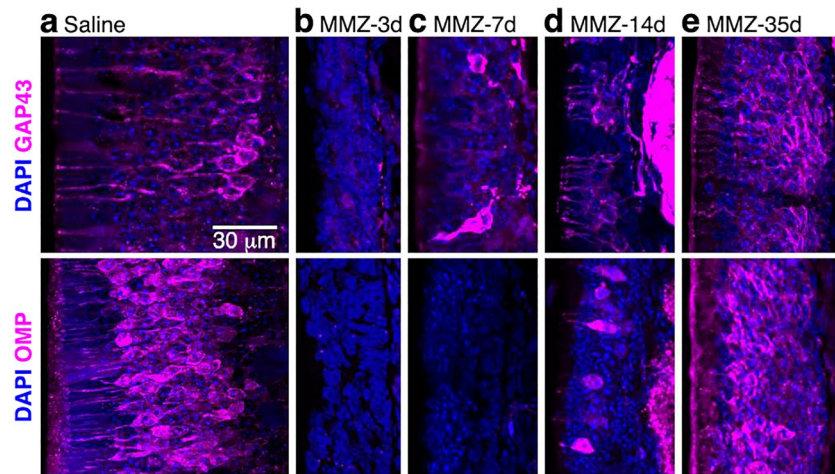


Figure 1. Repopulation of immature and mature OSNs after MMZ-mediated ablation. Images show single confocal optical sections of the septal olfactory epithelium of saline- and MMZ-treated mice. Top row: GAP43 staining of immature OSNs. Bottom row: OMP staining of mature OSNs. (a) 3 days post-saline treatment. (b–e) 3 days (b), 7 days (c), 14 days (d) and 35 days (e) post-MMZ treatment.

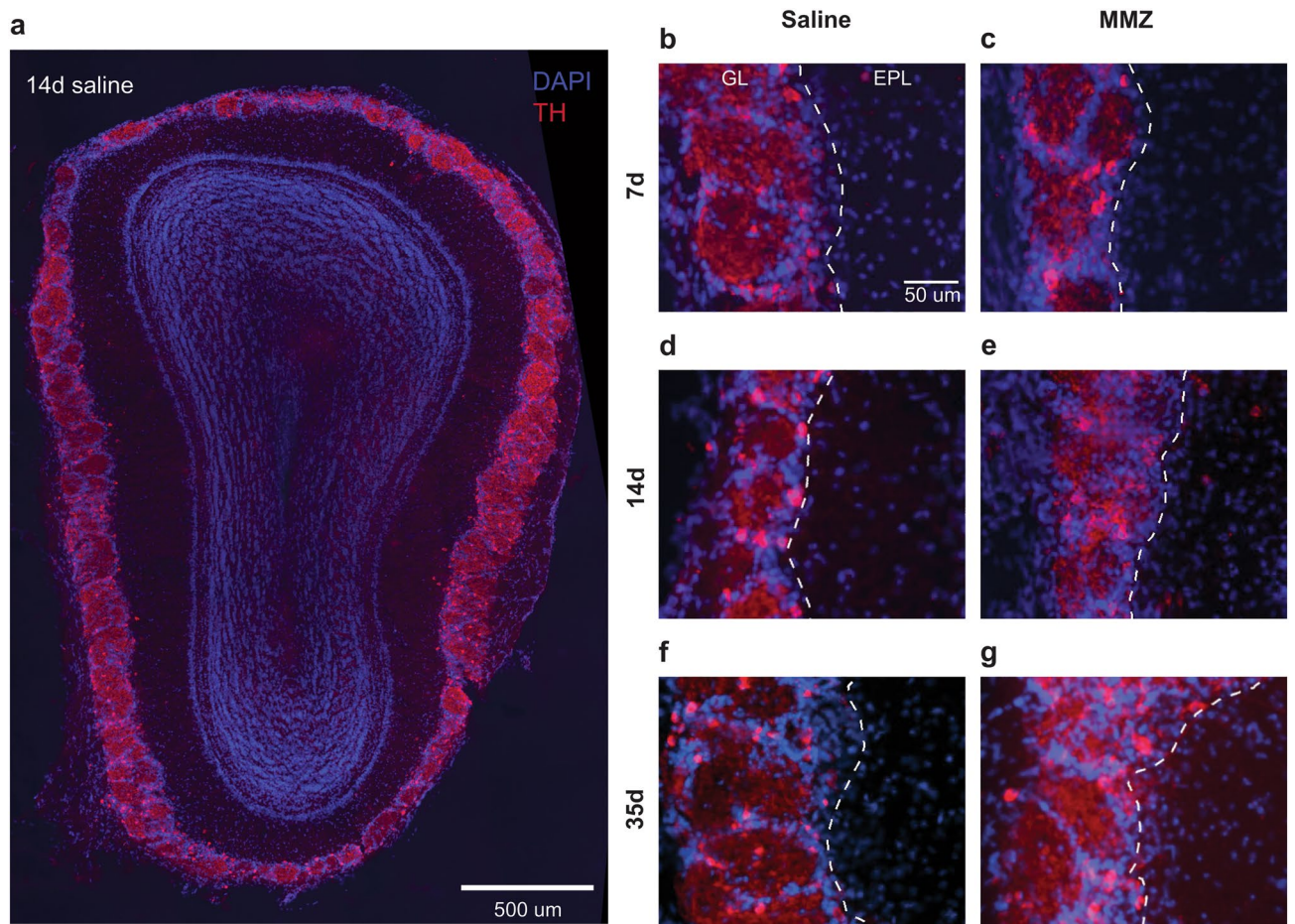


Figure 2. TH expression in the OB after MMZ treatment. (a) Coronal OB section from a saline-treated mouse showing TH expression primarily in the GL with scattered TH+ neurons in the EPL. (b–g) Enlarged views of the ventral GL and EPL from OBs stained 7, 14 or 35 days after treatment with saline (b,d,f) or MMZ (c,e,g).

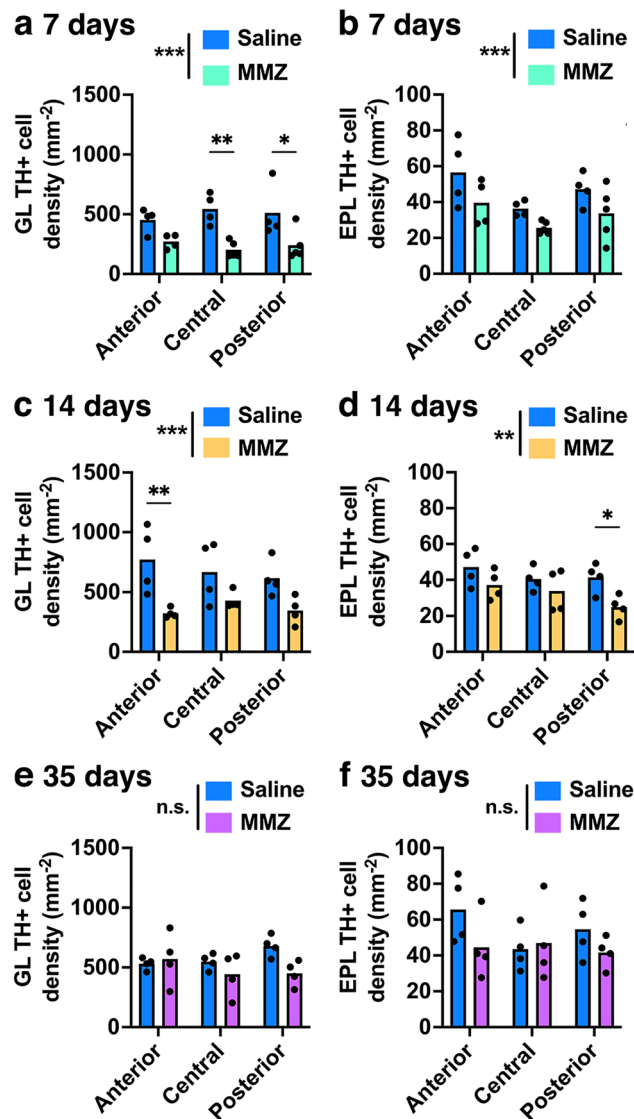


Figure 3. TH+ neuron density is reduced after MMZ treatment but recovers five weeks later. **(a)** GL TH+ neuron density is reduced 7 days after MMZ treatment (2-way ANOVA: $P < 0.001$, $F_{1,20} = 27.8$ for MMZ treatment, $P = 0.97$, $F_{2,20} = 0.028$ for A-P axis, $P = 0.45$, $F_{2,20} = 0.83$ for interaction). Pairwise comparisons showed a significant decrease after MMZ treatment in central and posterior sections (anterior $P = 0.16$, $t = 2.03$; central $P = 0.002$, $t = 4.00$; posterior $P = 0.014$, $t = 3.17$, Sidak's multiple comparisons). **(b)** EPL TH+ neuron density is reduced 7 days after MMZ treatment (2-way ANOVA: $P = 0.008$, $F_{1,20} = 8.82$ for MMZ treatment, $P = 0.024$, $F_{2,20} = 4.49$ for A-P axis, $P = 0.86$, $F_{2,20} = 0.15$ for interaction). **(c)** GL TH+ neuron density remains reduced at 14 days after MMZ treatment (2-way ANOVA: $P < 0.001$, $F_{1,18} = 19.5$ for MMZ treatment, $P = 0.68$, $F_{2,18} = 0.39$ for A-P axis, $P = 0.45$, $F_{2,18} = 0.83$ for interaction). Pairwise comparisons showed a significant decrease after MMZ treatment in anterior sections (anterior $P = 0.006$, $t = 3.59$; central $P = 0.21$, $t = 1.89$; posterior $P = 0.13$, $t = 2.16$, Sidak's multiple comparisons). **(d)** EPL TH+ neuron density remains reduced 14 days after MMZ treatment (2-way ANOVA: $P = 0.007$, $F_{1,18} = 9.26$ for MMZ treatment, $P = 0.15$, $F_{2,18} = 2.12$ for A-P axis, $P = 0.53$, $F_{2,18} = 0.66$ for interaction). Pairwise comparisons showed a significant decrease after MMZ treatment in posterior sections (anterior $P = 0.34$, $t = 1.58$; central $P = 0.67$, $t = 1.05$; posterior $P = 0.049$, $t = 2.64$, Sidak's multiple comparisons). **(e)** GL TH+ neuron density is similar 35 days after MMZ and saline treatment (2-way ANOVA: $P = 0.091$, $F_{1,18} = 3.19$ for MMZ treatment, $P = 0.56$, $F_{2,18} = 0.60$ for A-P axis, $P = 0.16$, $F_{2,18} = 2.02$). **(f)** EPL TH+ neuron density is similar 35 days after MMZ and saline treatment (2-way ANOVA: $P = 0.15$, $F_{1,18} = 2.26$ for MMZ treatment, $P = 0.49$, $F_{2,18} = 0.74$ for A-P axis, $P = 0.34$, $F_{2,18} = 1.13$ for interaction).

with MMZ or saline 7, 14 or 35 days earlier. Similar to previous reports^{4,28,31,33}, we found PV+ neurons throughout the EPL, with a lower density in the MCL and IPL, and very sparsely distributed in the GCL, in both saline and MMZ-treated mice (Fig. 4). We quantified the density of PV+ neurons in these layers, treating the MCL and IPL

as a single region of interest for analysis due to the limited thickness of these layers (Fig. 4b–g). We found no significant effect of either MMZ treatment or stage along the anterior–posterior axis on the density of PV+ neurons in any layer (Figs. 4, 5). Therefore, we concluded that MMZ treatment does not affect PV+ neuron survival or induce PV+ neurogenesis in adult mice.

However, we observed that the somatic morphology of PV+ neurons throughout the analyzed layers differed between MMZ- and saline-treated mice (Fig. 4b–e). To quantify this, we focused on the EPL, where PV+ neurons are numerous, and measured the soma area of a sample of PV+ neurons for each mouse. We found that PV+ neuron soma area was significantly reduced 7 and 14 days after MMZ treatment (Fig. 6a,b; 27% lower at 7 days and 28% lower at 14 days) but recovered to baseline by 35 days post-MMZ (Fig. 6c). Therefore, we concluded that OSN ablation alters OB PV+ neuron soma size. To determine the functional impact of reduced soma area, we determined the resultant change in input resistance and then used a leaky integrate and fire model to compare responses to square depolarizing current pulses in PV+ neurons. We found that rheobase was reduced and firing rate was significantly increased in the small soma area/higher input resistance PV+ neurons that are present 7–14 days after MMZ treatment (Fig. 6d). Hence, PV+ neurons are likely to have increased intrinsic excitability in 7–14-day post-MMZ mice.

Transient increase in CR+ neuron density in the GL and EPL 7 days after MMZ treatment

The effects of MMZ treatment on CR+ neuron survival or neurogenesis are unknown. In saline-treated mice, we found a high density of CR+ neurons in the GL and superficial GCL, a lower density in the EPL, and only scattered neurons in the MCL and IPL (Fig. 7), similar to previous reports^{43,61,62}. We therefore focused our quantitative analysis on CR-expressing neurons in the GL, EPL and GCL.

At the 7-day time point, we found that the density of CR+ neurons in the GL and EPL was consistently significantly higher in MMZ-treated than in saline-treated mice, throughout the anterior–posterior axis (Fig. 7b,c; Fig. 8a,b; 47% higher in the GL, 53% higher in the EPL). In contrast, CR+ neuron density in the GCL was similar in MMZ- and saline-treated mice at the 7-day time point (Fig. 8c). At the 14-day time point, there was no longer a difference in CR+ neuron density in the GL or EPL between MMZ- and saline-treated mice (Fig. 7d,e, Fig. 8d–e), but GCL CR+ neuron density was lower in MMZ-treated mice (Fig. 8f). In pairwise comparisons of sections at different stages through the OB, GCL CR+ neuron density was only significantly lower in MMZ-treated mice for anterior sections, although central and posterior sections showed a similar trend. At the 35-day time point, there was no difference in CR+ neuron density in any layer between MMZ- and saline-treated mice (Fig. 7f,g, Fig. 8g–i).

We also found differences in GCL CR+ neuron density along the anterior–posterior axis: density was higher in anterior than in posterior sections at both the 7-day (Fig. 8c) and the 14-day (Fig. 8f) time points, and there was a similar trend that did not reach statistical significance at the 35-day time point (Fig. 8i). To determine whether GCL CR+ neuron density may be non-uniform in the healthy OB, we further analyzed our data from saline-injected mice. We found a significant effect of anterior–posterior axis position ($P = 0.031$, $F_{2,22} = 4.09$) but not of time point after saline treatment ($P = 0.39$, $F_{2,22} = 0.98$; interaction $P = 0.93$, $F_{4,22} = 0.22$, 2-way ANOVA). Pairwise comparisons showed that GCL CR+ neuron density was higher in anterior than in posterior sections

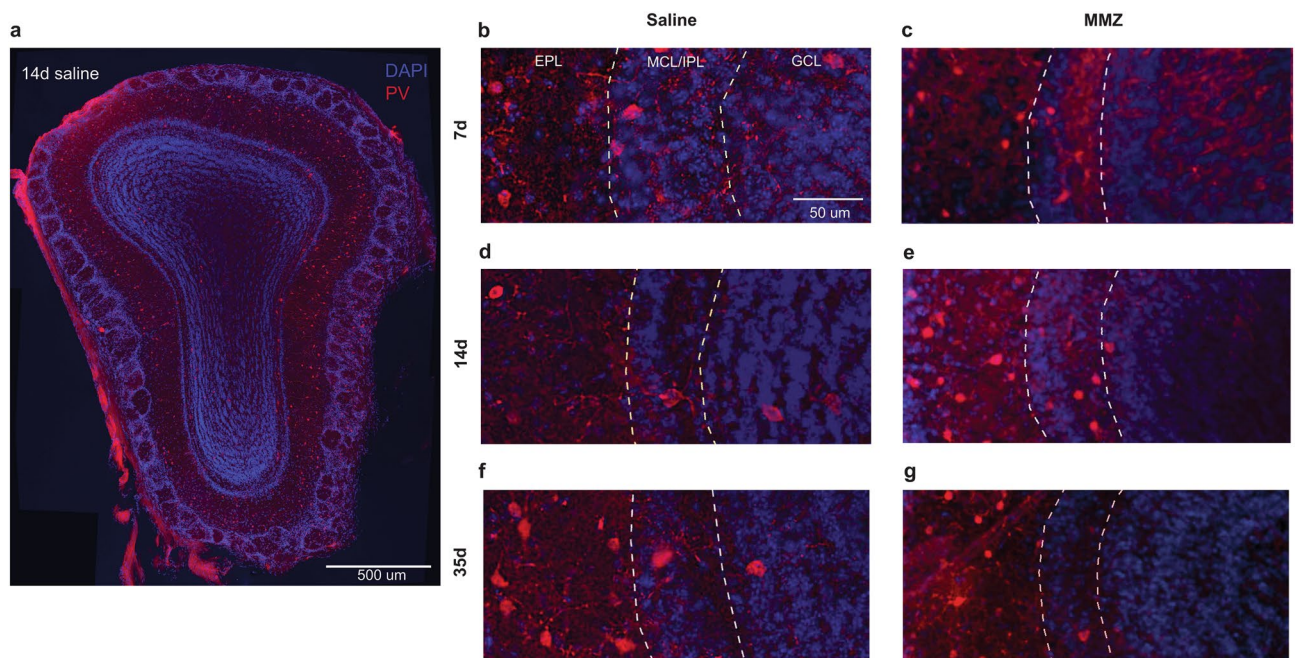


Figure 4. PV expression in the OB after MMZ treatment. (a) Coronal OB section from a saline-treated mouse showing PV expression predominantly in the EPL, with sparser expression in the MCL, IPL and GCL. (b–g) Enlarged views of the ventral EPL, MCL, IPL and GCL from OBs stained 7, 14 or 35 days after treatment with saline (b,d,f) or MMZ (c,e,g).

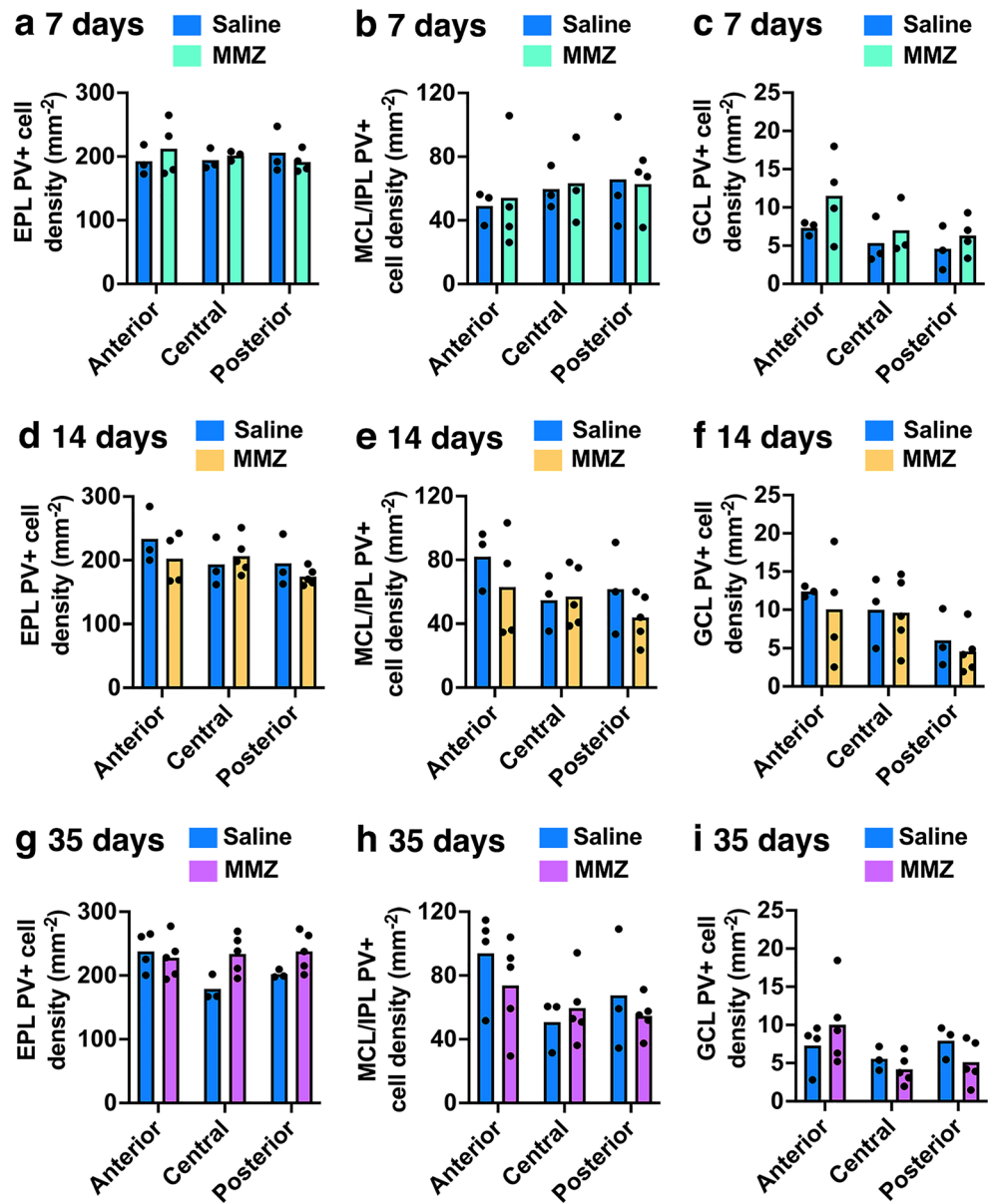


Figure 5. PV+OB neuron density is not affected by MMZ treatment. (a) EPL PV+ neuron density is similar 7 days after MMZ and saline treatment (2-way ANOVA: $P=0.75$, $F_{1,14}=0.11$ for MMZ treatment, $P=0.95$, $F_{2,14}=0.050$ for A-P axis, $P=0.53$, $F_{2,14}=0.66$ for interaction). (b) MCL and IPL PV+ neuron density is similar 7 days after MMZ and saline treatment (2-way ANOVA: $P=0.87$, $F_{1,14}=0.027$ for MMZ treatment, $P=0.65$, $F_{2,14}=0.45$ for A-P axis, $P=0.96$, $F_{2,14}=0.046$ for interaction). (c) GCL PV+ neuron density is similar 7 days after MMZ and saline treatment (2-way ANOVA: $P=0.14$, $F_{1,14}=2.49$ for MMZ treatment, $P=0.13$, $F_{2,14}=2.42$ for A-P axis, $P=0.76$, $F_{2,14}=0.28$ for interaction). (d) EPL PV+ neuron density is similar 14 days after MMZ and saline treatment (2-way ANOVA: $P=0.38$, $F_{1,17}=0.83$ for MMZ treatment, $P=0.20$, $F_{2,17}=1.77$ for A-P axis, $P=0.44$, $F_{2,17}=0.86$ for interaction). (e) MCL and IPL PV+ neuron density is similar 14 days after MMZ and saline treatment (2-way ANOVA: $P=0.25$, $F_{1,17}=1.41$ for MMZ treatment, $P=0.24$, $F_{2,17}=1.58$ for A-P axis, $P=0.61$, $F_{2,17}=0.51$ for interaction). (f) GCL PV+ neuron density is similar 14 days after MMZ and saline treatment (2-way ANOVA: $P=0.48$, $F_{1,17}=0.52$ for MMZ treatment, $P=0.056$, $F_{2,17}=3.44$ for A-P axis, $P=0.92$, $F_{2,17}=0.085$ for interaction). (g) EPL PV+ neuron density is similar 35 days after MMZ and saline treatment (2-way ANOVA: $P=0.094$, $F_{1,19}=3.11$ for MMZ treatment, $P=0.44$, $F_{2,19}=0.86$ for A-P axis, $P=0.20$, $F_{2,19}=1.75$ for interaction). (h) MCL and IPL PV+ neuron density is similar 35 days after MMZ and saline treatment (2-way ANOVA: $P=0.44$, $F_{1,19}=0.62$ for MMZ treatment, $P=0.071$, $F_{2,19}=3.05$ for A-P axis, $P=0.50$, $F_{2,19}=0.71$ for interaction). (i) GCL PV+ neuron density is similar 35 days after MMZ and saline treatment (2-way ANOVA: $P=0.72$, $F_{1,19}=0.13$ for MMZ treatment, $P=0.082$, $F_{2,19}=2.86$ for A-P axis, $P=0.22$, $F_{2,19}=1.64$ for interaction).

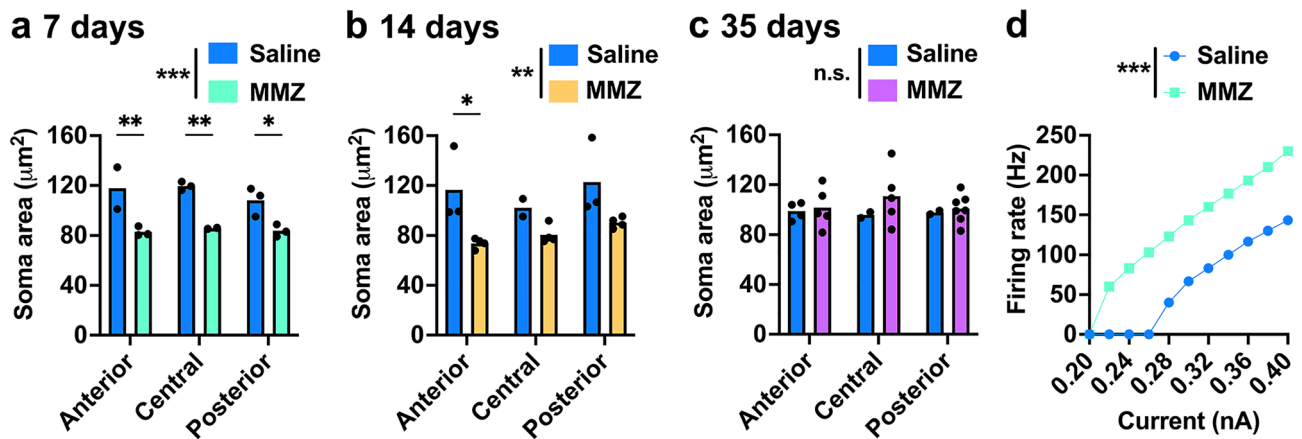


Figure 6. Reduced soma area of PV+ EPL neurons 7–14 days after MMZ treatment. **(a)** Soma area of EPL PV+ neurons is reduced 7 days after MMZ treatment (2-way ANOVA: $P < 0.001$, $F_{1,10} = 39.71$ for MMZ treatment, $P = 0.52$, $F_{2,10} = 0.69$ for A-P axis, $P = 0.63$, $F_{2,10} = 0.49$ for interaction). Pairwise comparisons showed a significant decrease after MMZ treatment in anterior, central and posterior sections (anterior $P = 0.034$, $t = 3.95$; central $P = 0.010$, $t = 3.83$; posterior $P = 0.008$, $t = 3.09$, Sidak's multiple comparisons). **(b)** Soma area of EPL PV+ neurons remains reduced 14 days after MMZ treatment (2-way ANOVA: $P = 0.001$, $F_{1,14} = 16.49$ for MMZ treatment, $P = 0.30$, $F_{2,14} = 1.32$ for A-P axis, $P = 0.58$, $F_{2,14} = 0.57$ for interaction). Pairwise comparisons showed a significant decrease after MMZ treatment in anterior sections (anterior $P = 0.017$, $t = 3.25$; central $P = 0.43$, $t = 1.44$; posterior $P = 0.078$, $t = 2.47$, Sidak's multiple comparisons). **(c)** Soma area of EPL PV+ neurons is similar 35 days after MMZ and saline treatment (2-way ANOVA: $P = 0.29$, $F_{1,19} = 1.17$ for MMZ treatment, $P = 0.89$, $F_{2,19} = 0.12$ for A-P axis, $P = 0.70$, $F_{2,19} = 0.37$ for interaction). **(d)** Predicted firing rate of PV+ neurons is higher in 7-day MMZ vs. 7-day saline treated mice from a leaky integrate and fire model (paired *t*-test: $P < 0.001$, $t = 9.21$).

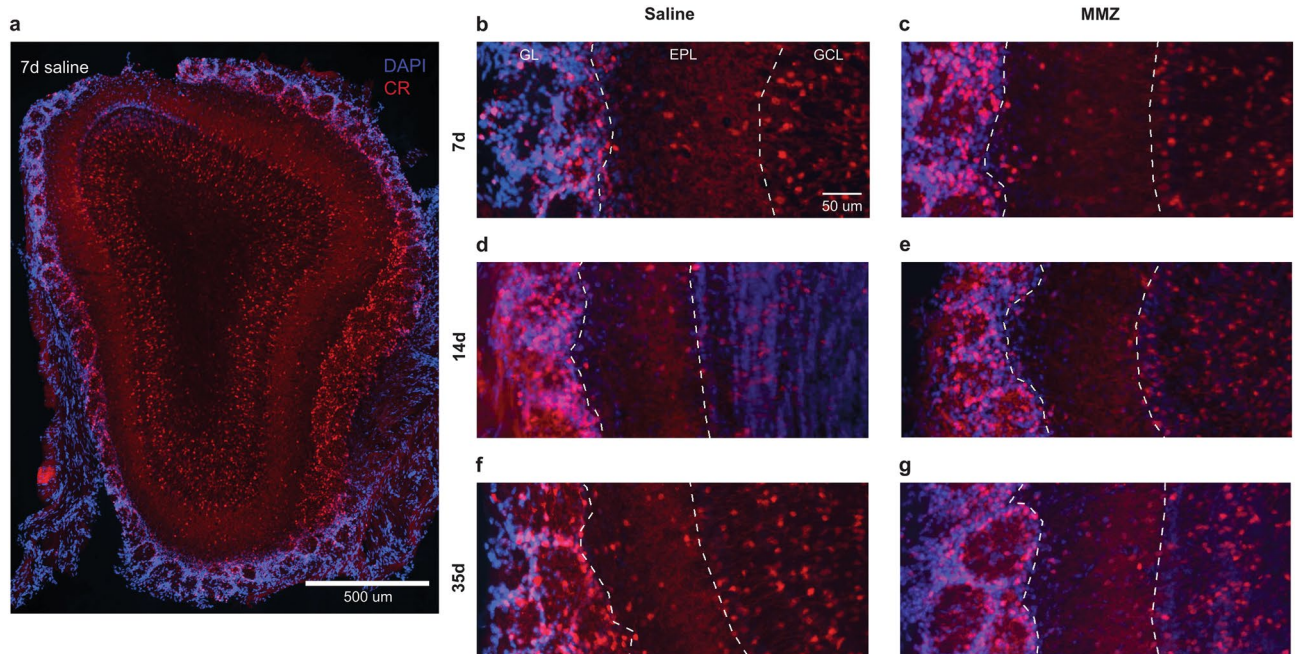


Figure 7. CR expression in the OB after MMZ treatment. **(a)** Coronal OB section from a saline-treated mouse showing CR expression throughout the GL, EPL and GCL. **(b–g)** Enlarged views of the ventral GL, EPL and GCL from OBs stained 7, 14 or 35 days after treatment with saline **(b,d,f)** or MMZ **(c,e,g)**.

($P = 0.024$, $q = 4.04$, Tukey's multiple comparisons) but found no difference between anterior vs. central or central vs. posterior sections. Therefore, our data suggest that there is a subtle gradient in GCL CR+ neuron density along the anterior–posterior axis of the OB.

We next focused on potential mechanisms that could underlie the transient increase in GL and EPL CR+ neuron density 7 days after MMZ treatment. CR+ neurons throughout the OB continue to be generated in adult mice^{28,35}; therefore, we asked whether enhanced CR+ neurogenesis could underlie the increase in CR+ neuron density that we observed. Approximately 90% of new juxtglomerular neurons generated in the SVZ take over

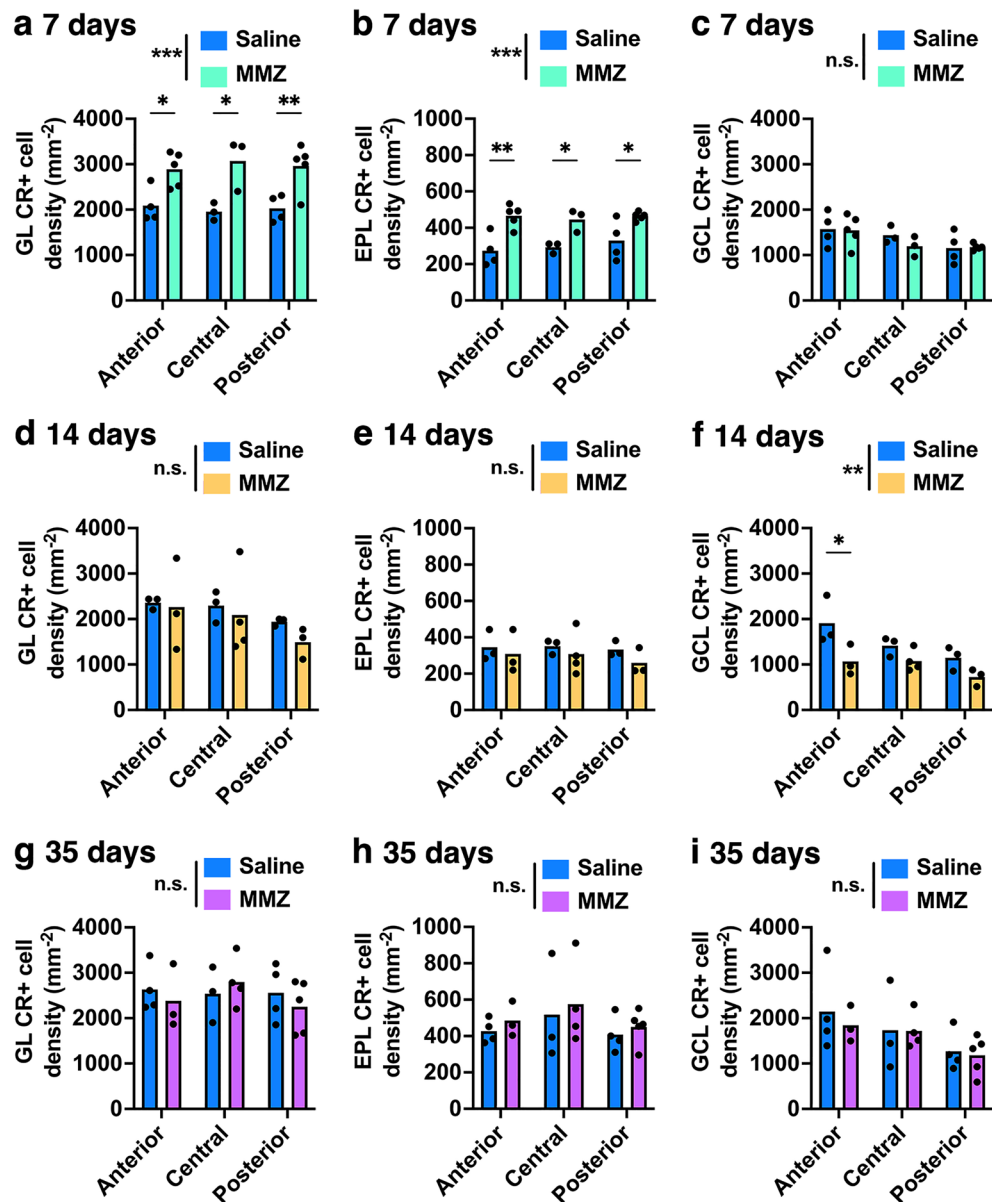


Figure 8. Transient increase in CR+ neuron density in the GL and EPL 7 days after MMZ treatment. (a) GL CR+ neuron density is increased 7 days after MMZ treatment (2-way ANOVA: $P < 0.001$, $F_{1,18} = 30.62$ for MMZ treatment, $P = 0.99$, $F_{2,18} = 0.006$ for A-P axis, $P = 0.77$, $F_{2,18} = 0.27$ for interaction). Pairwise comparisons showed a significant increase after MMZ treatment in anterior, central and posterior sections (anterior $P = 0.029$, $t = 2.89$; central $P = 0.011$, $t = 3.33$; posterior $P = 0.010$, $t = 3.38$, Sidak's multiple comparisons). (b) EPL CR+ neuron density is increased 7 days after MMZ treatment (2-way ANOVA: $P < 0.001$, $F_{1,18} = 30.42$ for MMZ treatment, $P = 0.67$, $F_{2,18} = 0.42$ for A-P axis, $P = 0.67$, $F_{2,18} = 0.40$ for interaction). Pairwise comparisons showed a significant increase after MMZ treatment in anterior, central and posterior sections (anterior $P = 0.002$, $t = 4.13$; central $P = 0.043$, $t = 2.70$; posterior $P = 0.030$, $t = 2.88$, Sidak's multiple comparisons). (c) GCL CR+ neuron density is similar 7 days after MMZ and saline treatment but there was a significant effect of position along the anterior–posterior axis (2-way ANOVA: $P = 0.49$, $F_{1,18} = 0.50$ for MMZ treatment, $P = 0.029$, $F_{2,18} = 4.35$ for A-P axis, $P = 0.66$, $F_{2,18} = 0.43$ for interaction). Pairwise comparisons showed that CR+ neuron density was lower in posterior than in anterior sections ($P = 0.027$, $t = 2.93$, Sidak's multiple comparisons). (d) GL CR+ neuron density is similar 14 days after MMZ and saline treatment (2-way ANOVA: $P = 0.41$, $F_{1,13} = 0.72$ for MMZ treatment, $P = 0.27$, $F_{2,13} = 1.47$ for A-P axis, $P = 0.89$, $F_{2,13} = 0.12$ for interaction). (e) EPL CR+ neuron density is similar 14 days after MMZ and saline treatment (2-way ANOVA: $P = 0.23$, $F_{1,13} = 1.57$ for MMZ treatment, $P = 0.77$, $F_{2,13} = 0.27$ for A-P axis, $P = 0.93$, $F_{2,13} = 0.072$ for interaction). (f) GCL CR+ neuron density is reduced 14 days after MMZ treatment (2-way ANOVA: $P = 0.003$, $F_{1,13} = 13.60$ for MMZ treatment, $P = 0.030$, $F_{2,13} = 4.68$ for A-P axis, $P = 0.35$, $F_{2,13} = 1.15$ for interaction). Pairwise comparisons showed a significant decrease after MMZ treatment in anterior sections (anterior $P = 0.018$, $t = 3.29$; central $P = 0.45$, $t = 1.41$; posterior $P = 0.33$, $t = 1.65$, Sidak's multiple comparisons), and that CR+ neuron density was lower in posterior than in anterior sections ($P = 0.028$, $t = 3.05$, Sidak's multiple comparisons). (g) GL CR+ neuron density is similar 35 days after MMZ and saline treatment (2-way ANOVA: $P = 0.70$, $F_{1,17} = 0.15$ for MMZ treatment, $P = 0.69$, $F_{2,17} = 0.37$ for A-P axis, $P = 0.62$, $F_{2,17} = 0.49$ for interaction). (h) EPL CR+ neuron density is similar 35 days after MMZ and saline treatment (2-way ANOVA: $P = 0.45$, $F_{1,17} = 0.60$ for MMZ treatment, $P = 0.36$, $F_{2,17} = 1.10$ for A-P axis, $P = 0.99$, $F_{2,17} = 0.006$ for interaction). (i) GCL CR+ neuron density is similar 35 days after MMZ and saline treatment (2-way ANOVA: $P = 0.62$, $F_{1,17} = 0.26$ for MMZ treatment, $P = 0.072$, $F_{2,17} = 3.09$ for A-P axis, $P = 0.91$, $F_{2,17} = 0.097$ for interaction).

7 days to reach the GL⁶³. However, it was possible that neurogenesis in the core of the OB itself, which preferentially produces CR+ neurons^{37,39–41}, could enable newly generated CR+ neurons to reach the GL and EPL within 7 days of MMZ injection. Therefore, we injected mice with either MMZ or saline, and then one day later with EdU, a thymidine analog that labels terminally dividing cells. We then quantified newborn CR+ neurons in the GL and EPL (Fig. 9a–d).

We found a two-fold increase in the density of CR+ EdU+ neurons in both the GL and the EPL in MMZ- vs. saline-treated mice (Fig. 9e). However, even in MMZ-treated mice, the density of CR+ EdU+ neurons was very low compared to the increase in CR+ neuron density due to MMZ treatment (GL: 6 mm^{-2} CR+ EdU+; 861 mm^{-2} increase in CR+ neuron density 7-days post-MMZ), and hence could not explain the overall increase in CR+ neuron density. We next determined the proportion of EdU-labeled cells that expressed CR but found no difference between MMZ-treated and control mice (Fig. 9f). Finally, we considered whether an increase in CR expression in existing GL and EPL neurons could underlie the increased CR+ neuron density that we observed. To estimate CR expression, we quantified the mean fluorescence intensity of CR staining in the GL and EPL, in images collected using identical acquisition settings. We found a significant increase in mean CR fluorescence intensity in the GL and EPL of MMZ-treated mice (Fig. 9g), with a 49% increase in the GL and a 192% increase in the EPL. We concluded that CR expression is increased 7 days after MMZ treatment.

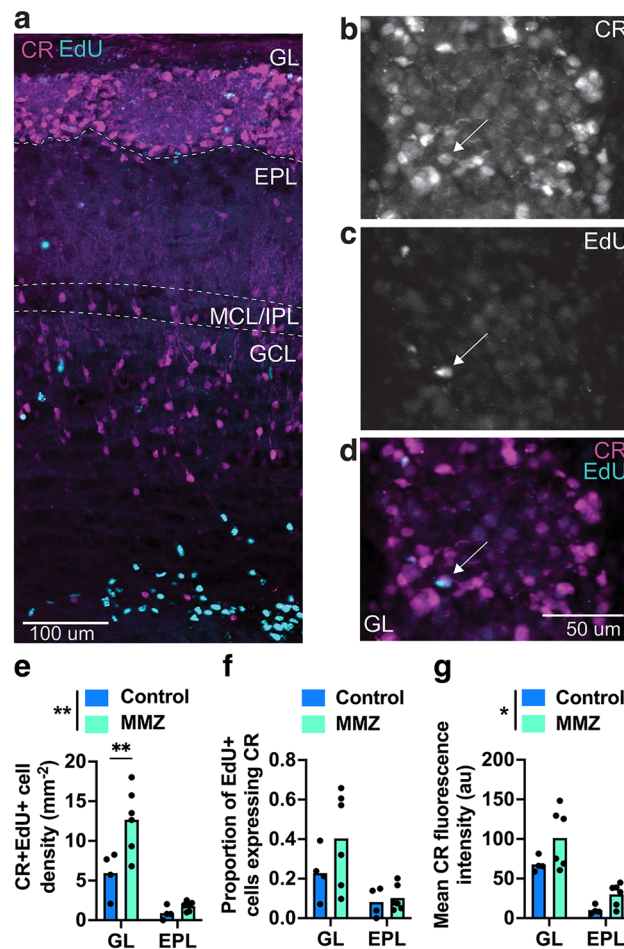


Figure 9. Increased CR expression rather than neurogenesis can account for the MMZ-mediated increase in CR+ neuron density. (a) Coronal OB section from a MMZ-treated mouse showing CR expression and EdU labeling throughout the OB 7 days after MMZ and 6 days after EdU treatment. (b–d) Enlarged view of a glomerulus showing CR expression (b), EdU labeling (c) and colocalization of CR and EdU ((d), arrow). (e) GL and EPL CR+ EdU+ neuron density is increased 7 days after MMZ treatment (2-way ANOVA: $P=0.006$, $F_{1,16}=9.96$ for MMZ treatment, $P<0.001$, $F_{1,16}=43.69$ for layer, $P=0.027$, $F_{1,16}=5.92$ for interaction, n for CR+ EdU+ neurons: 81 GL and 20 EPL from 6 MMZ-treated mice, and 34 GL and 6 EPL from 4 control mice). Pairwise comparisons showed a significant increase after MMZ treatment in the GL (GL $P=0.002$, $t=3.95$; EPL $P=0.85$, $t=0.51$, Sidak's multiple comparisons). (f) Proportion of EdU+ cells that express CR is not affected by MMZ treatment in the GL or EPL (2-way ANOVA: $P=0.18$, $F_{1,16}=1.92$ for MMZ treatment, $P=0.006$, $F_{1,16}=10.1$ for layer, $P=0.29$, $F_{1,16}=1.21$ for interaction, n for CR+ EdU+ neurons as in (e)). (g) GL and EPL CR fluorescence intensity is increased 7 days after MMZ treatment (2-way ANOVA: $P=0.021$, $F_{1,16}=6.50$ for MMZ treatment, $P<0.001$, $F_{1,16}=38.28$ for layer, $P=0.53$, $F_{1,16}=0.42$ for interaction).

Discussion

This is the first study to assess changes in OB interneuron density following MMZ-mediated OSN ablation of sensory input. We found cell type- and laminar-specific changes in OB interneuron populations. Most notably, the soma area of PV+ neurons was transiently reduced at 7–14 but not 35 days post-MMZ, and the density of CR+ neurons in the GL and EPL, but not the GCL, was transiently increased only at 7 days post-MMZ. This highlights the range of plasticity mechanisms employed within OB circuits following OE damage. It also raises important questions about the roles played by two very understudied types of neurons, CR+ PGCs and PV+ EPL interneurons, in the regenerating OB.

Changes in TH+ neuron density following MMZ treatment

In agreement with previous studies^{24–27,52,64,65}, we found that MMZ treatment resulted in complete ablation of OSNs within 3 days, with newly generated immature OSNs present within 7 days, newly generated mature OSNs present by 14 days, and substantial OSN repopulation by 35 days. The pattern of changes in TH+ neuron density that we saw also supports a dramatic reduction in sensory input, followed by gradual regeneration of sensory input between 7 and 35 days post-MMZ. It is highly likely that the reduction in TH+ neuron density in the GL and EPL arises from a combination of reduced TH expression and reduced DA neuron survival^{14–19}. Similarly, both activity-dependent recovery of TH expression and addition of newborn DA neurons are likely to contribute to the substantial recovery of TH+ neuron density by 35 days post-MMZ^{15,18,19}. Hence, we concluded that MMZ treatment enables the impact of bidirectional changes in OB sensory input to be assessed.

It is also interesting to compare the effects on TH+ neurons of MMZ treatment versus other methods that strongly reduce OB sensory input. Many early studies used chemical or surgical deafferentation methods, typically in neonates, but techniques to directly quantify TH expression were not available. The first study to assess the impact of adult-onset naris occlusion showed a gradual loss of TH+ immunoreactivity in the mouse GL, reaching a nadir at 3 weeks and persisting at least until 6 weeks after occlusion onset, but again these changes were not quantified¹⁴. The only other study to directly quantify TH+ neuron density found an 87% reduction in the GL of the occluded vs. unoccluded OB after P30–P60 naris cautery in rats⁴. Interestingly, however, the same study found only a ~35% reduction in GL TH optical density in the occluded vs. unoccluded OB. Another study in mice found 66% lower TH fluorescence intensity in the GL of occluded vs. unoccluded OBs at 3 and 6 weeks after naris cautery⁵. Studies employing naris occlusion via nose plugs⁶⁶ have reported 25–40% decreases in TH fluorescence intensity after 1–7 days compared to either the unoccluded OB or control mice^{67–69}. Hence, while a direct comparison that controls for other methodological differences would be needed to precisely address this issue, it appears that the magnitude of changes in TH expression is broadly similar after MMZ treatment vs. naris occlusion, at least at early time points. A comparison of recovery from MMZ treatment vs. naris occlusion would also be an interesting future direction.

Reduced soma size but unchanged density of PV+ neurons after MMZ treatment

PV+ neurons are normally generated predominantly during mouse embryonic development, with neurogenesis complete before P30²⁸. We therefore investigated PV+ neuron density to determine whether MMZ can reactivate neurogenesis of OB interneuron subtypes that are not normally generated during adulthood. However, we found no effect of MMZ treatment on PV+ neuron density in any OB layer at any time point examined. This indicates both that PV expression in the mouse OB is not activity-dependent, and that generation of PV+ neurons in the SVZ is not reactivated following MMZ treatment in mice. This may suggest more broadly that certain subtypes of SVZ-generated neurons cannot be produced in the adult brain, irrespective of experimental manipulations. There is considerable regional heterogeneity amongst SVZ neural stem cells, arising both from embryonic regional specification and differential transcription factor expression^{70,71}. PV+ neurons are generated from neural stem cells in both the pallial and lateral/medial ganglionic eminence regions of the telencephalic neuroepithelium (and the dorsal and lateral wall regions derived from them in the early postnatal SVZ)⁷². However, these same SVZ regions continue to generate new CR+ and TH+ OB interneurons in adult mice⁷², suggesting a finer level of control over developmental differences in interneuron subtype-specific neurogenesis.

Our findings differ from those of a previous study in rats, which found reduced EPL PV+ neuron density following naris occlusion beginning either perinatally or at P30⁴. The authors attributed this to an activity-dependent reduction in PV expression, for which there is precedent in rat binocular visual cortex following monocular deprivation⁷³, although they did not rule out cell death. One possible reason for this discrepancy is species-based differences. Notably, PV+ neuron density is much lower in rats (~10 neurons mm⁻²) than in mice (~200 neurons mm⁻², Fig. 6), and PV+ neurogenesis also peaks later in rats^{4,28,29}. PV+ neurons in the two species may also respond differently to disruption of sensory input. Another potential explanation is that PV expression is downregulated following naris occlusion but not MMZ treatment, a possibility that could be tested by directly comparing the two methods in the same species.

Our finding that PV+ neuron soma area is reduced by 28% at 7–14 days post-MMZ but recovers to baseline by 35 days, matching the time courses of OSN repopulation in the OE and of changes in TH+ neuron density, is intriguing. Indeed, naris occlusion in rats also significantly reduced PV+ soma area⁴. There is further precedent for activity-dependent changes in soma area in the olfactory, visual and auditory systems across species. In adult rats, mitral cell soma area decreased after 10 weeks of either deprivation of normal colony odor via rapid deodorized air flow, or constant exposure to cyclohexanone⁷⁴. PV+ relay neurons in the cynomolgus monkey lateral geniculate nucleus also have reduced soma area after chronic (14 month) loss of optic nerve input in a glaucoma model⁷⁵. Finally, soma area of neurons in auditory brainstem nuclei decreases within 24 h of cochlear ablation or tetrodotoxin (TTX)-mediated silencing of the vestibulocochlear nerve in gerbils⁷⁶. Of particular interest, soma area returned to baseline when activity was restored for 7 days following TTX-mediated silencing

in this model, matching the recovery of OB PV+ soma area that we saw. However, the molecular mechanisms underlying changes in soma area that we and others have observed, on timescales of days to weeks, are unclear. Neuronal volume must be tightly regulated in the face of changes in intracellular or extracellular osmolality to maintain excitability and normal cellular function^{77,78}. Neurons will shrink due to exposure to extracellular hypertonicity, but this triggers a volume regulatory increase in intracellular solute concentration, involving influx of sodium and chloride ions followed by organic osmolytes, to restore cell volume^{77,78}. However, because very little is known about how cells sense changes in their volume, or why manipulations of sensory input may cause neuronal shrinkage, it is unclear why volume regulatory mechanisms did not rapidly restore soma size in PV+ neurons after MMZ treatment.

The consequences of reduced soma area for neuronal function are unclear. Moderate cell shrinkage, unlike cell swelling, appears not to significantly disrupt cellular architecture⁷⁸, suggesting that the smaller PV+ neurons present at 7–14 days post-MMZ may still be functional. Input capacitance is directly proportional to membrane surface area, while input resistance is inversely proportional to membrane surface area⁷⁹. Hence, the 27% decrease in soma area that we found for PV+ neurons at 7 days post-MMZ would result in reduced capacitance and increased input resistance, which would be expected to increase excitability. This was corroborated by our integrate-and-fire model, which, while based purely on anatomical data, suggested a reduced rheobase and increased firing rate for PV+ neurons following MMZ treatment. This could markedly increase inhibition of OB output neurons³². However, while sensory input is absent or weak during the early stages of recovery, as after MMZ treatment, this would predominantly act to dampen spontaneous activity of OB output neurons. In addition, an important caveat is that we did not determine whether MMZ treatment also alters the dendritic morphology of PV+ neurons, which could also impact their excitability. Directly testing the impact of 7–14 days of MMZ treatment on both PV+ neuron excitability and PV-mediated inhibition of OB output neurons is an interesting future direction.

Transient changes in CR+ neuron density following MMZ treatment

Our most striking finding in this study is the transient and laminar-specific increase in GL and EPL CR+ neuron density at 7 days post-MMZ, which is no longer seen at 14 days post-MMZ. There are several potential mechanisms that could account for this transient increase. The first possibility is enhanced integration of CR+ neurons in the GL and EPL. While 7 days is very short for new SVZ-derived neurons to reach the GL, with 90% of newborn juxtglomerular neurons retrovirally labeled in the RMS arriving after 7 days post-injection⁶³, CR+ neurons are also generated in the OB core^{36,37}, enabling them to reach the GL within 7 days. Indeed, we found a twofold increase in the density of newborn EdU+ CR+ neurons in the GL and EPL at 7 days post-MMZ, suggesting that OB core neurogenesis may be upregulated. However, the increase in the absolute number of CR+ EdU+ neurons was very small (6.7 mm^{-2} in the GL) relative to the overall increase in CR+ neuron density (861 mm^{-2} in the GL). A single EdU injection one day after MMZ treatment may label only a fraction of the additional CR+ neurons that are being added, and EdU-mediated toxicity⁸⁰ could also reduce the fraction of the newly added population that is labeled. However, it seems unlikely that we labeled less than 0.8% of the newly generated CR+ neurons that reached the GL by 7 days post-MMZ. Furthermore, OB core neurogenesis generates similar proportions of CR+ PGCs and GCs^{36,37}, but GCL CR+ neuron density was not increased at 7 days post-MMZ. Hence, we concluded that enhanced neurogenesis could not account for the rapid increase in CR+ density in the GL and EPL following MMZ treatment.

A second possibility is that juxtglomerular neuron fate specification was altered. We found no difference in the proportion of EdU-labeled cells that expressed CR, suggesting that fate determination of neurons generated immediately after MMZ treatment is not altered. A more systematic study of newborn neurons pre-labeled with EdU at different time points prior to MMZ treatment would be required to conclusively answer the question of whether neuroblasts that were already en route to their final destination preferentially differentiated into CR+ PGCs. However, it is notable that a previous study found no difference in the proportions of CR+, CB+ and TH+ cells amongst neurons labeled with BrdU either before or after naris occlusion⁵, suggesting that fate determination is unlikely to be altered by loss of sensory input.

Finally, we considered whether CR expression might increase, such that cells that were previously undetectable by immunohistochemistry now expressed detectable levels of CR. Indeed, mean CR fluorescence intensity increased significantly in the GL and EPL. Hence, we concluded that increased CR expression in GL and EPL neurons is a significant contributor to the transiently increased CR+ neuron density observed 7 days post-MMZ. What are the functional effects of increased CR expression? As a hexa-EF-hand calcium binding protein with high cooperativity, CR buffers calcium, especially at high intracellular calcium concentrations, and may also function as a calcium sensor, undergoing calcium-dependent conformational changes⁸¹. CR knockout increased presynaptic release probability in cerebellar parallel fibers⁸² and increased excitability in cerebellar granule cells⁸³. However, the effects of increased CR expression on CR+ PGCs, which are poorly connected with the local network and rarely fire action potentials^{46,47}, are difficult to predict. Interestingly, it has been proposed that CR+ PGCs remain in an immature state, perhaps providing a reserve population that can be recruited when required by the circuit⁴⁷. Hence, it is intriguing to speculate that increased CR expression may be indicative of greater integration of CR+ PGCs into the glomerular network in responses to the loss of sensory input induced by MMZ treatment.

Data availability

Data are publicly available at <https://doi.org/https://doi.org/10.5281/zenodo.12774850>⁸⁴.

Received: 14 May 2024; Accepted: 26 July 2024

Published online: 01 August 2024

References

- Altman, J. Autoradiographic and histological studies of postnatal neurogenesis. IV. Cell proliferation and migration in the anterior forebrain, with special reference to persisting neurogenesis in the olfactory bulb. *J. Comp. Neurol.* **137**, 433–457 (1969).
- Lois, C. & Alvarez-Buylla, A. Long-distance neuronal migration in the adult mammalian brain. *Science* **264**, 1145–1148 (1994).
- Luskin, M. B. Restricted proliferation and migration of postnatally generated neurons derived from the forebrain subventricular zone. *Neuron* **11**, 173–189 (1993).
- Philpot, B. D., Lim, J. H. & Brunjes, P. C. Activity-dependent regulation of calcium-binding proteins in the developing rat olfactory bulb. *J. Comp. Neurol.* **387**, 12–26 (1997).
- Bastien-Dionne, P., David, L. S., Parent, A. & Saghatelian, A. Role of sensory activity on chemospecific populations of interneurons in the adult olfactory bulb. *J. Comp. Neurol.* **518**, 1847–1861 (2010).
- Banerjee, A. *et al.* An interglomerular circuit gates glomerular output and implements gain control in the mouse olfactory bulb. *Neuron* **87**, 193–207 (2015).
- Liu, S., Puche, A. C. & Shipley, M. T. The interglomerular circuit potently inhibits olfactory bulb output neurons by both direct and indirect pathways. *J. Neurosci.* **36**, 9604–9617 (2016).
- Liu, S., Plachez, C., Shao, Z., Puche, A. & Shipley, M. T. Olfactory bulb short axon cell release of GABA and dopamine produces a temporally biphasic inhibition–excitation response in external tufted cells. *J. Neurosci.* **33**, 2916–2926 (2013).
- Shao, Z., Liu, S., Zhou, F., Puche, A. C. & Shipley, M. T. Reciprocal inhibitory glomerular circuits contribute to excitation–inhibition balance in the mouse olfactory bulb. *eNeuro* **6**, ENEURO.0048-19.2019 (2019).
- Vaaga, C. E., Yorgason, J. T., Williams, J. T. & Westbrook, G. L. Presynaptic gain control by endogenous cotransmission of dopamine and GABA in the olfactory bulb. *J. Neurophysiol.* **117**, 1163–1170 (2017).
- Ennis, M. *et al.* Dopamine D2 receptor-mediated presynaptic inhibition of olfactory nerve terminals. *J. Neurophysiol.* **86**, 2986–2997 (2001).
- Hsia, A. Y., Vincent, J.-D. & Lledo, P.-M. Dopamine depresses synaptic inputs into the olfactory bulb. *J. Neurophysiol.* **82**, 1082–1085 (1999).
- McGann, J. P. Presynaptic inhibition of olfactory sensory neurons: New mechanisms and potential functions. *Chem. Senses* **38**, 459–474 (2013).
- Baker, H., Morel, K., Stone, D. & Maruniak, J. Adult naris closure profoundly reduces tyrosine hydroxylase expression in mouse olfactory bulb. *Brain Res.* **614**, 109–116 (1993).
- Baker, H., Kawano, T., Margolis, F. & Joh, T. Transneuronal regulation of tyrosine hydroxylase expression in olfactory bulb of mouse and rat. *J. Neurosci.* **3**, 69–78 (1983).
- Nadi, N. S. *et al.* Chemical deafferentation of the olfactory bulb: Plasticity of the levels of tyrosine hydroxylase, dopamine and norepinephrine. *Brain Res.* **213**, 365–377 (1981).
- Kawano, T. & Margolis, F. L. Transsynaptic regulation of olfactory bulb catecholamines in mice and rats. *J. Neurochem.* **39**, 342–348 (1982).
- Angelova, A., Tiveron, M.-C., Loizeau, M. D., Cremer, H. & Platel, J.-C. Effects of sensory deprivation on glomerular interneurons in the mouse olfactory bulb: Differences in mortality and phenotypic adjustment of dopaminergic neurons. *Front. Cell. Neurosci.* **17**, 1170170 (2023).
- Sawada, M. *et al.* Sensory input regulates spatial and subtype-specific patterns of neuronal turnover in the adult olfactory bulb. *J. Neurosci.* **31**, 11587–11596 (2011).
- Caggiano, M., Kauer, J. S. & Hunter, D. D. Globose basal cells are neuronal progenitors in the olfactory epithelium: A lineage analysis using a replication-incompetent retrovirus. *Neuron* **13**, 339–352 (1994).
- Leung, C. T., Coulombe, P. A. & Reed, R. R. Contribution of olfactory neural stem cells to tissue maintenance and regeneration. *Nat. Neurosci.* **10**, 720–726 (2007).
- Iwai, N., Zhou, Z., Roop, D. R. & Behringer, R. R. Horizontal basal cells are multipotent progenitors in normal and injured adult olfactory epithelium. *Stem Cells* **26**, 1298–1306 (2008).
- Cheetham, C. E., Park, U. & Belluscio, L. Rapid and continuous activity-dependent plasticity of olfactory sensory input. *Nat. Commun.* **7**, 10729 (2016).
- Kikuta, S. *et al.* Sensory deprivation disrupts homeostatic regeneration of newly generated olfactory sensory neurons after injury in adult mice. *J. Neurosci.* **35**, 2657–2673 (2015).
- Browne, L. P., Crespo, A. & Grubb, M. S. Rapid presynaptic maturation in naturally regenerating axons of the adult mouse olfactory nerve. *Cell Rep.* **41**, 111750 (2022).
- Blanco-Hernández, E., Valle-Leija, P., Zomosa-Signoret, V., Drucker-Colín, R. & Vidaltamayo, R. Odor memory stability after reinnervation of the olfactory bulb. *PLoS One* **7**, e46338 (2012).
- Huang, J. S. *et al.* Immature olfactory sensory neurons provide behaviourally relevant sensory input to the olfactory bulb. *Nat. Commun.* **13**, 6194 (2022).
- Batista-Brito, R., Close, J., Machold, R. & Fishell, G. The distinct temporal origins of olfactory bulb interneuron subtypes. *J. Neurosci.* **28**, 3966–3975 (2008).
- Li, X. *et al.* The transcription factor Sp8 is required for the production of parvalbumin-expressing interneurons in the olfactory bulb. *J. Neurosci.* **31**, 8450–8455 (2011).
- Toida, K., Kosaka, K., Heizmann, C. W. & Kosaka, T. Synaptic contacts between mitral/tufted cells and GABAergic neurons containing calcium-binding protein parvalbumin in the rat olfactory bulb, with special reference to reciprocal synapses between them. *Brain Res.* **650**, 347–352 (1994).
- Toida, K., Kosaka, K., Heizmann, C. W. & Kosaka, T. Electron microscopic serial-sectioning/reconstruction study of parvalbumin-containing neurons in the external plexiform layer of the rat olfactory bulb. *Neuroscience* **72**, 449–466 (1996).
- Kato, H. K., Gillet, S. N., Peters, A. J., Isaacson, J. S. & Komiyama, T. Parvalbumin-expressing interneurons linearly control olfactory bulb output. *Neuron* **80**, 1218–1231 (2013).
- Kosaka, T. *et al.* An aspect of the organization of the GABAergic system in the rat main olfactory bulb: laminar distribution of immunohistochemically defined subpopulations of GABAergic neurons. *Brain Res.* **411**, 373–378 (1987).
- Kosaka, T. & Kosaka, K. Heterogeneity of parvalbumin-containing neurons in the mouse main olfactory bulb, with special reference to short-axon cells and β IV-spectrin positive dendritic segments. *Neurosci. Res.* **60**, 56–72 (2008).
- Marchis, S. D. *et al.* Generation of distinct types of periglomerular olfactory bulb interneurons during development and in adult mice: Implication for intrinsic properties of the subventricular zone progenitor population. *J. Neurosci.* **27**, 657–664 (2007).
- Acosta, F. J. F. *et al.* Morphological diversity of calretinin interneurons generated from adult mouse olfactory bulb core neural stem cells. *Front. Cell Dev. Biol.* **10**, 932297 (2022).
- Defferali, Ç. *et al.* Neural stem cells in the adult olfactory bulb core generate mature neurons in vivo. *Stem Cells* **39**, 1253–1269 (2021).
- Hack, M. A. *et al.* Neuronal fate determinants of adult olfactory bulb neurogenesis. *Nat. Neurosci.* **8**, 865–872 (2005).
- Gritti, A. *et al.* Multipotent neural stem cells reside into the rostral extension and olfactory bulb of adult rodents. *J. Neurosci.* **22**, 437–445 (2002).

40. Fukushima, N., Yokouchi, K., Kawagishi, K. & Moriizumi, T. Differential neurogenesis and gliogenesis by local and migrating neural stem cells in the olfactory bulb. *Neurosci. Res.* **44**, 467–473 (2002).
41. Liu, Z. & Martin, L. J. Olfactory bulb core is a rich source of neural progenitor and stem cells in adult rodent and human. *J. Comp. Neurol.* **459**, 368–391 (2003).
42. Panzanelli, P., Fritschy, J. M., Yanagawa, Y., Obata, K. & Sassoè-Pognetto, M. GABAergic phenotype of periglomerular cells in the rodent olfactory bulb. *J. Comp. Neurol.* **502**, 990–1002 (2007).
43. Parrish-Aungst, S., Shipley, M. T., Erdelyi, F., Szabo, G. & Puche, A. C. Quantitative analysis of neuronal diversity in the mouse olfactory bulb. *J. Comp. Neurol.* **501**, 825–836 (2007).
44. Whitman, M. C. & Greer, C. A. Adult-generated neurons exhibit diverse developmental fates. *Dev. Neurobiol.* **67**, 1079–1093 (2007).
45. Ninkovic, J., Mori, T. & Götz, M. Distinct modes of neuron addition in adult mouse neurogenesis. *J. Neurosci.* **27**, 10906–10911 (2007).
46. Iseppe, A. F., Pignatelli, A. & Belluzzi, O. Calretinin-periglomerular interneurons in mice olfactory bulb: Cells of few words. *Front. Cell. Neurosci.* **10**, 231 (2016).
47. Benito, N. *et al.* A pool of postnatally generated interneurons persists in an immature stage in the olfactory bulb. *J. Neurosci.* **38**, 9870–9882 (2018).
48. Najac, M. *et al.* Intraglomerular lateral inhibition promotes spike timing variability in principal neurons of the olfactory bulb. *J. Neurosci.* **35**, 4319–4331 (2015).
49. Hardy, D., Malvaut, S., Breton-Provencher, V. & Saghatelian, A. The role of calretinin-expressing granule cells in olfactory bulb functions and odor behavior. *Sci. Rep.* **8**, 9385 (2018).
50. Goedhart, J. Studentsourcing—Aggregating and reusing data from a practical cell biology course. *PLOS Comput. Biol.* **20**, e1011836 (2024).
51. Schindelin, J. *et al.* Fiji: An open-source platform for biological-image analysis. *Nat. Methods* **9**, 676–682 (2012).
52. Tsai, L. & Barnea, G. A critical period defined by axon-targeting mechanisms in the murine olfactory bulb. *Science* **344**, 197–200 (2014).
53. Genter, M. B., Owens, D. M. & Deamer, N. J. Distribution of microsomal epoxide hydrolase and glutathione S-transferase in the rat olfactory mucosa: Relevance to distribution of lesions caused by systemically-administered olfactory toxicants. *Chem. Senses* **20**, 385–392 (1995).
54. Genter, M. B., Deamer, N. J., Blake, B. L., Wesley, D. S. & Levi, P. E. Olfactory toxicity of methimazole: Dose-response and structure-activity studies and characterization of flavin-containing monooxygenase activity in the Long-Evans rat olfactory mucosa. *Toxicol. Pathol.* **23**, 477–486 (1995).
55. Chen, M. *et al.* Wnt-responsive Lgr5+ globose basal cells function as multipotent olfactory epithelium progenitor cells. *J. Neurosci.* **34**, 8268–8276 (2014).
56. Brann, J. H., Ellis, D. P., Ku, B. S., Spinazzi, E. F. & Firestein, S. Injury in aged animals robustly activates quiescent olfactory neural stem cells. *Front. Neurosci.* **9**, 367 (2015).
57. Kosaka, K. & Kosaka, T. Chemical properties of type 1 and type 2 periglomerular cells in the mouse olfactory bulb are different from those in the rat olfactory bulb. *Brain Res.* **1167**, 42–55 (2007).
58. Kohwi, M. *et al.* A subpopulation of olfactory bulb GABAergic interneurons is derived from Emx1- and Dlx5/6-expressing progenitors. *J. Neurosci.* **27**, 6878–6891 (2007).
59. Baker, H. *et al.* Olfactory bulb dopamine neurons survive deafferentation-induced loss of tyrosine hydroxylase. *Neuroscience* **11**, 605–615 (1984).
60. Halasz, N. *et al.* Transmitter histochemistry of the rat olfactory bulb. I. Immunohistochemical localization of monoamine synthesizing enzymes. Support for intrabulbar, periglomerular dopamine neurons. *Brain Res.* **126**, 455–474 (1977).
61. Jacobowitz, D. M. & Winsky, L. Immunocytochemical localization of calretinin in the forebrain of the rat. *J. Comp. Neurol.* **304**, 198–218 (1991).
62. Kosaka, K. *et al.* Chemically defined neuron groups and their subpopulations in the glomerular layer of the rat main olfactory bulb. *Neurosci. Res.* **23**, 73–88 (1995).
63. Kovalchuk, Y. *et al.* In vivo odourant response properties of migrating adult-born neurons in the mouse olfactory bulb. *Nat. Commun.* **6**, 6349 (2015).
64. Bergman, U., Östergren, A., Gustafson, A.-L. & Brittebo, E. Differential effects of olfactory toxicants on olfactory regeneration. *Arch. Toxicol.* **76**, 104–112 (2002).
65. Sakamoto, T., Kondo, K., Kashio, A., Suzukawa, K. & Yamasoba, T. Methimazole-induced cell death in rat olfactory receptor neurons occurs via apoptosis triggered through mitochondrial cytochrome c-mediated caspase-3 activation pathway. *J. Neurosci. Res.* **85**, 548–557 (2007).
66. Cummings, D., Henning, H. & Brunjes, P. Olfactory bulb recovery after early sensory deprivation. *J. Neurosci.* **17**, 7433–7440 (1997).
67. Byrne, D. J., Lipovsek, M., Crespo, A. & Grubb, M. S. Brief sensory deprivation triggers plasticity of dopamine-synthesising enzyme expression in genetically labelled olfactory bulb dopaminergic neurons. *Eur. J. Neurosci.* **56**, 3591–3612 (2022).
68. Galliano, E. *et al.* Brief sensory deprivation triggers cell type-specific structural and functional plasticity in olfactory bulb neurons. *J. Neurosci.* **41**, 2135–2151 (2021).
69. Grier, B. D., Belluscio, L. & Cheetham, C. E. Olfactory sensory activity modulates microglial-neuronal interactions during dopaminergic cell loss in the olfactory bulb. *Front. Cell. Neurosci.* **10**, 178 (2016).
70. Chaker, Z., Codega, P. & Doetsch, F. A mosaic world: Puzzles revealed by adult neural stem cell heterogeneity. *Wiley Interdiscip. Rev. Dev. Biol.* **5**, 640–658 (2016).
71. Fiorelli, R., Azim, K., Fischer, B. & Raineteau, O. Adding a spatial dimension to postnatal ventricular-subventricular zone neurogenesis. *Development* **142**, 2109–2120 (2015).
72. Young, K. M., Fogarty, M., Kessar, N. & Richardson, W. D. Subventricular zone stem cells are heterogeneous with respect to their embryonic origins and neurogenic fates in the adult olfactory bulb. *J. Neurosci.* **27**, 8286–8296 (2007).
73. Cellerino, A., Siciliano, R., Domenici, L. & Maffei, L. Parvalbumin immunoreactivity: A reliable marker for the effects of monocular deprivation in the rat visual cortex. *Neuroscience* **51**, 749–753 (1992).
74. Panhuber, H., Mackay-Sim, A. & Laing, D. G. Prolonged odor exposure causes severe cell shrinkage in the adult rat olfactory bulb. *Dev. Brain Res.* **31**, 307–311 (1987).
75. Yücel, Y. H., Zhang, Q., Weinreb, R. N., Kaufman, P. L. & Gupta, N. Atrophy of relay neurons in magno- and parvocellular layers in the lateral geniculate nucleus in experimental glaucoma. *Investig. Ophthalmol. Vis. Sci.* **42**, 3216–3222 (2001).
76. Pasic, T. R., Moore, D. R. & Rubel, E. W. Effect of altered neuronal activity on cell size in the medial nucleus of the trapezoid body and ventral cochlear nucleus of the gerbil. *J. Comp. Neurol.* **348**, 111–120 (1994).
77. Toney, G. M. Regulation of neuronal cell volume: From activation to inhibition to degeneration. *J. Physiol.* **588**, 3347–3348 (2010).
78. Wilson, C. S. & Mongin, A. A. Cell volume control in healthy brain and neuropathologies. *Curr. Top. Membr.* **81**, 385–455 (2018).
79. Koch, C. *Biophysics of Computation: Information Processing in Single Neurons* (Oxford University Press, 1999).
80. Platel, J.-C. *et al.* Neuronal integration in the adult mouse olfactory bulb is a non-selective addition process. *Elife* **8**, e44830 (2019).
81. Schwaller, B. Calretinin: From a “simple” Ca²⁺ buffer to a multifunctional protein implicated in many biological processes. *Front. Neuroanat.* **8**, 3 (2014).

82. Schmidt, H. *et al.* Nanodomain coupling at an excitatory cortical synapse. *Curr. Biol.* **23**, 244–249 (2013).
83. Gall, D. *et al.* Altered neuronal excitability in cerebellar granule cells of mice lacking calcitonin. *J. Neurosci.* **23**, 9320–9327 (2003).
84. Kunkhyen, T. *et al.* Source data for Cell type- and layer-specific plasticity of olfactory bulb interneurons following olfactory sensory neuron ablation (Version 1.0) [Data]. Zenodo. <https://doi.org/10.5281/zenodo.12774850> (2024).

Acknowledgements

We thank Gerry Hammond (University of Pittsburgh) for use of the Nikon A1R confocal microscope and members of the Cheetham lab for helpful discussions.

Author contributions

Conceptualization: TK, CEJC. Methodology: TK, TRB, SPRB, CEJC. Investigation: TK, TRB, SPRB, PP, ANR. Software: AG, CEJC. Formal analysis: TK, TRB, SPRB, PP, ANR, CEJC. Visualization: SPRB, CEJC. Writing—original draft: CEJC. Writing: review & editing: TK, TRB, SPRB, ANR, CEJC. Supervision: TK, CEJC. Funding acquisition: TK, CEJC. Project administration: CEJC.

Funding

The funding was supported by National Institute on Deafness and other Communication Disorders, R01DC018516, and National Institute on Deafness and Other Communication Disorders, F32DC018431.

Competing interests

The authors declare no competing interests.

Additional information

Correspondence and requests for materials should be addressed to C.E.J.C.

Reprints and permissions information is available at www.nature.com/reprints.

Publisher's note Springer Nature remains neutral with regard to jurisdictional claims in published maps and institutional affiliations.



Open Access This article is licensed under a Creative Commons Attribution-NonCommercial-NoDerivatives 4.0 International License, which permits any non-commercial use, sharing, distribution and reproduction in any medium or format, as long as you give appropriate credit to the original author(s) and the source, provide a link to the Creative Commons licence, and indicate if you modified the licensed material. You do not have permission under this licence to share adapted material derived from this article or parts of it. The images or other third party material in this article are included in the article's Creative Commons licence, unless indicated otherwise in a credit line to the material. If material is not included in the article's Creative Commons licence and your intended use is not permitted by statutory regulation or exceeds the permitted use, you will need to obtain permission directly from the copyright holder. To view a copy of this licence, visit <http://creativecommons.org/licenses/by-nc-nd/4.0/>.

© The Author(s) 2024